Rayleigh Mixture Model for Plaque Characterization in Intravascular Ultrasound

José C. Seabra*, *Member, IEEE*, Francesco Ciompi, Oriol Pujol, Josepa Mauri, Petia Radeva, *Member, IEEE*, and João Sanches, *Member, IEEE*

Abstract—Vulnerable plaques are the major cause of carotid and coronary vascular problems, such as heart attack or stroke. A correct modeling of plaque echomorphology and composition can help the identification of such lesions. The Rayleigh distribution is widely used to describe (nearly) homogeneous areas in ultrasound images. Since plaques may contain tissues with heterogeneous regions, more complex distributions depending on multiple parameters are usually needed, such as Rice, K or Nakagami distributions. In such cases, the problem formulation becomes more complex, and the optimization procedure to estimate the plaque echomorphology is more difficult. Here, we propose to model the tissue echomorphology by means of a mixture of Rayleigh distributions, known as the Rayleigh mixture model (RMM). The problem formulation is still simple, but its ability to describe complex textural patterns is very powerful. In this paper, we present a method for the automatic estimation of the RMM mixture parameters by means of the expectation maximization algorithm, which aims at characterizing tissue echomorphology in ultrasound (US). The performance of the proposed model is evaluated with a database of *in vitro* intravascular US cases. We show that the mixture coefficients and Rayleigh parameters explicitly derived from the mixture model are able to accurately describe different plaque types and to significantly improve the characterization performance of an already existing methodology.

Index Terms—Echomorphology, intravascular ultrasound (IVUS), plaque characterization, Rayleigh mixture model (RMM), vulnerable plaque.

*J. C. Seabra is with the Institute for Systems and Robotics, Instituto Superior Técnico, Universida de Técnica de Lisboa, 1049-001 Lisboa, Portugal (e-mail: jseabra@isr.ist.utl.pt).

F. Ciompi was with the Computer Vision Center, Universitat Autónoma de Barcelona, 08193 Barcelona, Spain. They are now with the Departement Matematica Aplicada i Analisis, Universitat de Barcelona, 08007 Barcelona, Spain (e-mail: f.ciompi@gmail.com).

O. Pujol and P. Radeva are with the Computer Vision Center, Universitat Autónoma de Barcelona, 08193 Barcelona, Spain, and also with the Departement Matematica Aplicada i Analisis, Universitat de Barcelona, 08007 Barcelona, Spain (e-mail: oriol@maia.ub.es; petia@cvc.uab.es).

J. Mauri is with the University Hospital "Germans Trias i Pujol," 08916 Badalona, Spain (e-mail: mauritri@gmail.com).

J. Sanches is with the Institute for Systems and Robotics, Instituto Superior Técnico, Universidade Técnica de Lisboa, 1049-001 Lisboa, Portugal (e-mail: jmrs@isr.ist.utl.pt).

Color versions of one or more of the figures in this paper are available online at http://ieeexplore.ieee.org.

Digital Object Identifier 10.1109/TBME.2011.2106498

I. INTRODUCTION

VULNERABLE plaques are lesions presenting high risk of rupture, possibly leading to brain stroke or heart attack [1]. Although vulnerable plaque is a concept well accepted as a clinical entity with potential harmful consequences, from the point of view of its echomorphology and pathological evolution, it is not yet well understood. Hence, it is important to objectively characterize the plaque echomorphology to identify this kind of lesions, thus, allowing the development or refinement of methods for risk prediction and potentially suggesting different therapies.

In medical ultrasound (US), a transmitted ultrasonic pulse interacts with an anatomical region providing information about internal tissue structures [2]. The backscattered (received) signal is corrupted by a characteristic granular pattern noise called speckle [3], which depends on the number of scatterers (reflectors) as well as their size. As pointed out in [4], these features can be considered as tissue histological descriptors.

Intravascular US (IVUS) is an imaging technique that allows to clearly assess the arterial wall internal echomorphology. The technical procedure of acquiring IVUS data consists in introducing a catheter, carrying a rotating US emitter inside the vessel. During rotation, a piezoelectric transducer transmits US waves and collects the reflected components that are afterward converted into electrical signals (A-lines) and sampled by an analog-to-digital converter. The IVUS image obtained by processing the received echoes is a 360° tomographic view of the inner arterial walls [see Fig. 1(a)]. Thus, IVUS is considered a suitable technique for *in vivo* characterization of the coronary plaques composition.

This paper intends to model the atherosclerotic plaque through the analysis of the envelope backscattered IVUS data. For this purpose, an hypothetical model is considered, where a scanned tissue sample suffers from a certain number of scattering phenomena, as depicted in Fig. 2.

The most common model for speckle formation, known as fully developed speckle, considers a tissue or region composed of a large number of scatterers, acting as echo reflectors. These scatterers arise from inhomogeneity and structures approximately equal to or smaller in size than the wavelength of the US, such as tissue parenchyma, where there are changes in acoustic impedance on a microscopic level within the tissue. It is recognized that under fully developed speckle, pixel intensities in envelope images are well modeled by Rayleigh probability density functions (PDFs) [3], [5]. An application example is given in [6], where the morphological properties of the arterial vessel on IVUS images are modeled by means of a Rayleigh
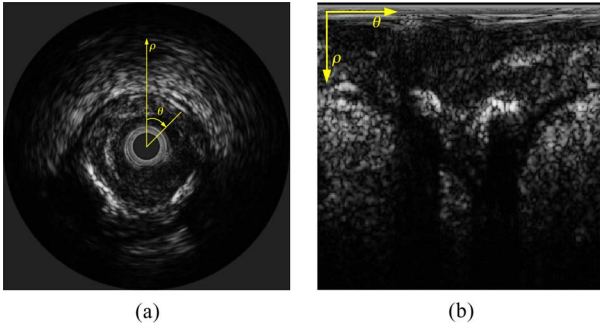
Fig. 1.   (a) Cross-sectional Intravascular US (IVUS) image (in cartesian coordinates) and (b) corresponding polar representation; ρ represents the depth in the tissue and θ the position (angle) in the rotation of the probe.
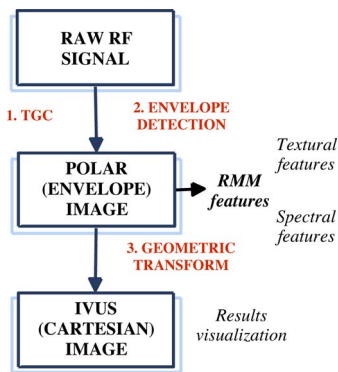

Fig. 2.   Tissue acoustic model (different scattering phenomena may occur).

distribution in a fully automatic method for luminal contour segmentation. When this condition does not hold, other more complex parametric models, such as K [7], Rician [8], homodyned-K [9], and Nakagami [10], are suitable to describe the data.

The motivation to use the Rayleigh, single parameter, distribution comes from the fact that the regions defining atherosclerotic tissue are piecewise homogeneous and do not present strong scatterers nor edges, as it happens across the rest of the image, where other speckle conditions are verified and other statistical models are more convenient. These other models (Rice, K, or Nakagami distributions) depend on a large number of parameters, which makes the estimation of tissue echomorphology a hard task.

Plaque echomorphology may result from different types of components, spatial organization, and complexity, which determine different scattering phenomena, where the Rayleigh distribution would be a reasonable approximation but a compound statistical model would be more appropriate. Hence, the description of tissue echomorphology may be tackled with complex distributions, depending on multiple parameters or with a mixture of simple distributions. Following the latter approach, this paper uses a combination of Rayleigh distributions—*Rayleigh mixture model* (RMM)—estimated with the *expectation maximization* (EM) algorithm, thus, making the modeling of tissue echomorphology a rather simple but fast and robust process.

The RMM consists of a technique to describe a particular data distribution by linearly combining different PDFs. Up to our knowledge, the RMM was never used for tissue characterization in US, although, these models have been successfully employed in other fields, such as in underwater acoustics and speech-processing problems [11].

The contributions of this paper can be summarized as follows. First, in Section II-A, we provide a comprehensive mathematical formulation of the mixture model, which makes use of the EM algorithm for estimating the coefficients and Rayleigh parameters of the mixture PDF. Second, the adequacy of the proposed model to describe the envelope US data is evaluated using a validated IVUS data set of different plaque types (see Section III-C). Moreover, the RMM is applied for modeling plaques as monolithic objects, i.e., by considering all the pixels enclosed in the plaque. The features explicitly obtained from the mixture model (cf. Section II-B are used to investigate the discriminative power of the model for identifying different tissue types, namely, fibrotic, lipidic, and calcified tissues. Then, in Section III-D, the ability of the RMM for pixelwise classification of plaque composition is evaluated when using only the new features and when combining them with other texture and spectral features recently proposed [12]. Finally, we investigate the significance of the obtained classification improvement when using the RMM features (cf. Section III-E and III-F).

II.   METHODS

This section aims at providing the mathematical description for estimating the mixture coefficients (weights) and the Rayleigh parameters associated with each mixture component (distribution) using the EM method applied to US data.

A.   Rayleigh Mixture Model

Let $\mathbf{Y} = \{y_i\}, 1 \leq i \leq N$, be a set of pixel intensities of a given region of interest (plaque) from an US image. Pixel intensities are considered random variables, which are described by the following mixture of L distributions:

$$p(y_i|\mathbf{\Psi}) = \sum_{j=1}^{L} \theta_j p(y_i|\sigma_j) \tag{1}$$

where σ_j is the parameter of the Rayleigh PDF $p(y_i|\sigma_j)$ given by

$$p(y_i|\sigma_j) = \frac{y_i}{\sigma_j^2} e^{-\frac{y_i^2}{2\sigma_j^2}} \tag{2}$$

and the parameters $\mathbf{\Psi} = (\theta_1, \ldots, \theta_L, \sigma_1, \ldots, \sigma_L)$ are the coefficients (θ_j) and Rayleigh parameters (σ_j) of the mixture, respectively. The condition $\sum_{j=1}^{L} \theta_j = 1$ must hold to guarantee that $p(y_i|\mathbf{\Psi})$ is a true distribution function.

The parameters σ_j associated with the pixel intensity y_i characterize the acoustic properties of the tissue at the ith location [13]. The effect of changing σ in the shape of the distribution and thus in the image intensity is illustrated in Fig. 3. The joint distribution of the pixel intensities, considered independent and identically distributed (i.i.d.), is given by
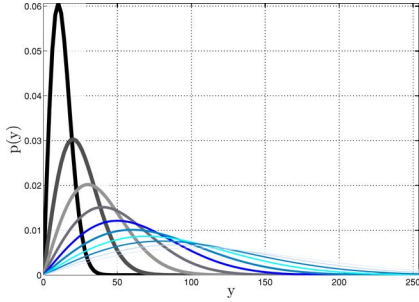
Fig. 3. *Rayleigh* PDFs generated with parameter $10^2 < \sigma < 10^3$ (from darker to lighter curves).

$$p(\mathbf{Y}|\mathbf{\Psi}) = \prod_i^N p(y_i|\mathbf{\Psi}). \qquad (3)$$

The goal is to estimate $\mathbf{\Psi}$ by maximizing the *likelihood* function such that

$$\hat{\mathbf{\Psi}}_{\mathrm{ML}} = \arg\max_{\mathbf{\Psi}} \mathcal{L}(\mathbf{Y}, \mathbf{\Psi}) \qquad (4)$$

where

$$\mathcal{L}(\mathbf{Y}, \mathbf{\Psi}) = \log p(\mathbf{Y}|\mathbf{\Psi}) = \sum_{i=1}^N \log\left(\sum_{j=1}^L \theta_j p_j(y_i|\sigma_j)\right). \qquad (5)$$

The maximization of (5) is a difficult task because it consists of a logarithmic function of a sum of terms. To overcome this difficulty, the EM [14] method is used, where a set of hidden variables are introduced, $\mathbf{K} = \{k_i\}$ with $k_i \in \{1, \ldots, L\}$. The value of $k_i = j$ informs us about the mixture component j that generated the ith pixel intensity y_i, with probability $p(y_i|\sigma_{k_i})$ defined in (2).

Each nth iteration of the EM method is composed of two steps:

1) *E step:* where the *expectation* of the new *likelihood* function $\mathcal{L}(\mathbf{Y}, \mathbf{K}, \mathbf{\Psi})$ is computed with respect to $\mathbf{K}$

$$\mathcal{Q}(\mathbf{Y}, \mathbf{\Psi}^n, \mathbf{\Psi}) = E_{\mathbf{K}}\left[\mathcal{L}(\mathbf{Y}, \mathbf{K}(\mathbf{\Psi}^n), \mathbf{\Psi})\right] \qquad (6)$$

and

2) *M step:* where a new estimate of $\mathbf{\Psi}$, $\mathbf{\Psi}^{n+1}$, is obtained by maximizing the function $\mathcal{Q}$

$$\mathbf{\Psi}^{n+1} = \arg\max_{\mathbf{\Psi}} \mathcal{Q}(\mathbf{Y}, \mathbf{\Psi}^n, \mathbf{\Psi}). \qquad (7)$$

These two steps alternate until convergence is achieved, which happens when $|\mathbf{\Psi}^{n+1} - \mathbf{\Psi}^n|$ is lower than a stopping criterion (ξ) set to 10^{-3}. The new *likelihood* function is

$$\mathcal{L}(\mathbf{Y}, \mathbf{K}, \mathbf{\Psi}) = \log p(\mathbf{Y}, \mathbf{K}|\mathbf{\Psi}) = \sum_{i=1}^N \log p(y_i, k_i|\mathbf{\Psi})$$

$$= \sum_{i=1}^N \log p(y_i|\sigma_{k_i}) + \log \underbrace{p(k_i|\sigma_{k_i})}_{\theta_{k_i}} \qquad (8)$$

where $p(y_i|\sigma_{k_i})|_{k_i=j}$, defined in (2), is the k_ith component of the RMM and θ_{k_i} is the mixture coefficient associated with the k_ith

component. The maximization of (8) is impossible because the hidden variables $\mathbf{K}$ are not known. Therefore, the *expectation* with respect to $\mathbf{K}$ is computed as follows:

$$\mathcal{Q}(\mathbf{\Psi}, \hat{\mathbf{\Psi}}) = E_{\mathbf{K}}\left[\mathcal{L}(\mathbf{Y}, \mathbf{K}, \mathbf{\Psi})|\mathbf{Y}, \hat{\mathbf{\Psi}}\right]$$

$$= \sum_{i=1}^N E_{k_i}\left[\log p(y_i|\sigma_{k_i}) + \log p(k_i|\sigma_{k_i})\right]$$

$$= \sum_{i=1}^N \sum_{j=1}^L \gamma_{i,j}[\log p(y_i|\sigma_j) + \log \theta_j] \qquad (9)$$

where $\hat{\mathbf{\Psi}} = (\hat{\theta}_1, \ldots, \hat{\theta}_L, \hat{\sigma}_1, \ldots, \hat{\sigma}_L)$ is the previous estimation of the parameters, and $\gamma_{i,j}$ is the distribution of the unobserved variables, which is defined as follows:

$$\gamma_{i,j} = p(k_i = j|y_i, \hat{\mathbf{\Psi}}) = \frac{p(y_i|\hat{\sigma}_j)p(k_i = j)}{p(y_i|\hat{\mathbf{\Psi}})} \qquad (10)$$

where

$$\sum_{j=1}^L \gamma_{i,j} = 1. \qquad (11)$$

In (10), $p(y_i|\hat{\sigma}_j)$ is computed, as in (2), $p(k_i = j) = \hat{\theta}_j$, and by definition

$$p(y_i|\hat{\mathbf{\Psi}}) = \sum_{j=1}^L p(y_i|\hat{\sigma}_j). \qquad (12)$$

The *likelihood* function (9) contains two independent terms, one depending on θ_j and the other on σ_j; thus, the $\mathcal{Q}$ function can be minimized independently with respect to each one. The log-*likelihood* function in (9) can be rewritten by separating the terms that depend exclusively on θ_j and σ_j, and considering (2) resulting in

$$\mathcal{Q}(\mathbf{\Psi}, \hat{\mathbf{\Psi}}) = \sum_{i=1}^N \sum_{j=1}^L \gamma_{i,j}\log(\theta_j) + \sum_{i=1}^N \sum_{j=1}^L \gamma_{i,j}\left[\log\left(\frac{y_i}{\sigma_j^2}\right) - \frac{y_i^2}{2\sigma_j^2}\right]. \qquad (13)$$

Hence, the $\mathcal{Q}$ function can now be minimized independently with respect to θ_j and σ_j. Let us focus on the term of (13), depending on θ. The method of *Lagrange multipliers* [15], particularly useful in mathematical optimization, provides a strategy for finding the solution of this term, subject to a normalization constraint given by

$$\sum_{j=1}^L \theta_j = 1. \qquad (14)$$

Moreover, it yields a necessary condition for optimality in constrained problems [15]. By introducing a new variable (λ) and solving the partial derivative of the term, depending on θ, leads to

$$\frac{\partial}{\partial\theta_r}\left[\sum_{i=1}^N \sum_{r=1}^L \gamma_{i,r}\log(\theta_r) + \lambda\left(\sum_r \theta_r - 1\right)\right] = 0 \qquad (15)$$

which results in

$$\sum_{i=1}^{N} \gamma_{i,r} = -\lambda \theta_r. \tag{16}$$

If we sum both sides of (16) over r

$$\sum_{i=1}^{N} \underbrace{\sum_{r=1}^{L} \gamma_{i,r}}_{(11)} = -\lambda \underbrace{\sum_{r=1}^{L} \theta_r}_{(14)} \tag{17}$$

we get that $N = -\lambda$, which finally yields

$$\hat{\theta}_r = \frac{1}{N} \sum_{i=1}^{N} \gamma_{i,r}. \tag{18}$$

The mixture parameters σ_j are found by deriving the term in (13) that depends exclusively of σ_j and setting it to 0 as follows:

$$\frac{\partial}{\partial \sigma_r} \left[\sum_{i=1}^{N} \sum_{r=1}^{L} \gamma_{i,r} \left(\log \left(\frac{y_i}{\sigma_r^2} \right) - \frac{y_i^2}{2\sigma_r^2} \right) \right] = 0 \tag{19}$$

which is easily solved for σ_r to obtain

$$\hat{\sigma}_r = \frac{\sum_{i=1}^{N} \gamma_{i,r}(y_i^2/2)}{\sum_{i=1}^{N} \gamma_{i,r}} = \sqrt{\frac{1}{N} \sum_{i=1}^{N} \gamma_{i,r} \frac{y_i^2}{2}}. \tag{20}$$

The EM algorithm is initialized with L uniformly weighted coefficients $\mathbf{\Theta} = \{\theta_j\} = 1/L$, while the mixture parameters are assigned with the *maximum likelihood* (ML) estimator [16], $\hat{\sigma}_{\mathrm{ML}} = \sqrt{(1/2N) \sum_{i=1}^{N} y_i^2}$. The initial choice of components was set arbitrarily to $L = 10$. However, when $|\sigma_m - \sigma_n| < \epsilon = 1$ (*ad hoc* setting), meaning that two distributions are closely similar, with $(m \neq n) = \{1, \dots, L\}$, then $\sigma_j = (\sigma_m + \sigma_n)/2$, $\theta_j = \theta_m + \theta_n$, and the number of mixture components is decreased by 1. This constraint assures stability of the RMM, particularly, for modeling plaque echomorphology. Preliminary observations allowed to verify that $L = 10$ is an overestimated guess (excessive number of mixture components), which also has implications in the computational cost of the RMM algorithm. The study of an effective input value for the number of mixture components to be used in the plaque characterization problem is further investigated in Sections III-C and III-D.

B. RMM Features

The technique for estimating the RMM parameters and coefficients using the EM method has been presented. We are further interested in assessing the adequacy of the proposed model to describe different types of tissue, and particularly, to characterize the atherosclerotic plaque.

In order to apply the RMM technique on a classification problem, the RMM must be estimated locally, and descriptive features must be extracted. Given the envelope image (cf. Section III-A), local RMM features are computed by means of a $K_s \times K_s$ sliding window, moved by a step of $S = (3/4)K_s$. For each position, a $2L + 1$ feature array is obtained and presented in the following manner: the first L positions correspond to the Rayleigh parameters sorted in ascending order, followed

by the L respective coefficients, arranged accordingly. The last position corresponds to the number of effective (distinct) mixture components $\tau = \{1, \dots, L\}$, which is found, as described in Section II-A.

III. EXPERIMENTAL RESULTS

In this section, we first provide a description of the methods used to acquire and process the IVUS data, and we briefly introduce the classification framework adopted for tuning the RMM algorithm and performing plaque characterization. Then, two distinct experiments are conducted: the first studies the adequacy of the RMM for describing different tissue types. This experiment is designated as *monolithic description* since the mixture model is estimated by considering all the pixels enclosed in the plaque. The second experiment refers to plaque characterization made pixel-by-pixel (hence, called *plaque local characterization*), where the RMM is applied not to the entire plaque, but to each processing block centered at the pixel to be characterized. Given this, the ability of the RMM for local characterization of plaque composition is evaluated when using only the RMM features and when combining them with other texture and spectral features recently proposed in [12]. Finally, we present a statistical analysis that supports the relevance of the obtained classification improvement when using the RMM features.

A. In Vitro Data Processing

The adequacy of the proposed RMM to describe real tissue types is evaluated through an *in vitro* study of atherosclerotic plaques from an IVUS database. The IVUS data set has been recently presented in [12] and consists of eight postmortem arteries, resulting in 45 frames with 24 fibrotic, 12 lipidic, and 31 calcified plaques. This data set, composed of 67 plaques, has been validated by histological analysis.

Real-time RF data acquisition has been performed with the Galaxy II IVUS Imaging System (Boston Scientific) with a catheter Atlantis SR Pro 40 MHz (Boston Scientific). To collect and store the RF data, the imaging system has been connected to a workstation equipped with a 12-bit Acquiris acquisition card with a sampling rate of 200 MHz. The RF data for each frame is arranged in a data matrix of $N \times M$ samples, where $M = 1024$ is the number of samples per *A-line*, and $N = 256$ is the number of positions assumed by the rotational US probe.

The information encoded in the visual appearance of tissues naturally represents a relevant feature for their description. However, during acquisition, the imaging parameters of the IVUS equipment are typically changed to enhance tissue visualization. Hence, parameters like contrast depth and brightness can change from patient to patient or even from image to image. When the IVUS images are then processed for feature extraction, this fact may generate noncomparable features.

To avoid the aforementioned errors and to produce normalized data, the used data follows a rigorous acquisition protocol, where the IVUS images have been directly reconstructed from the raw RF signals, rather than using the ones produced by the IVUS equipment. For this purpose, we follow an image
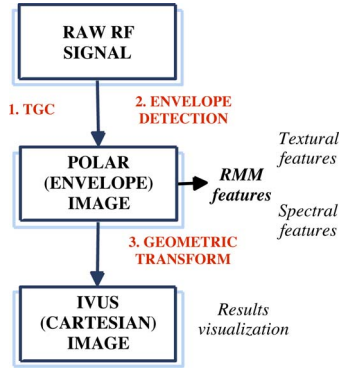
Fig. 4. IVUS data processing (see text for details). RMM, textural, and spectral features are extracted from polar image.

reconstruction algorithm [12], [17] outlined in Fig. 4. The reconstruction operations are applied to the RF data, where a preliminary time gain compensation (TGC) function is used

$$\text{TGC}(r) = 1 - e^{-\beta r} \tag{21}$$

where $\beta = \ln 10^{\alpha f/20}$, α is the attenuation coefficient for biological soft tissues ($\alpha \approx 0.8$ dB/MHz·cm for $f = 40$MHz [18]), f is the central frequency of the transducer in megahertz, and r is the radial distance from the catheter in centimeters. After signal compensation, using TGC, and envelope detection, using the Hilbert transform, the signal-processing procedure described in [12] is applied to get the polar representation of the IVUS image, or simply the envelope image, resulting in a noncompressed, 256×256 pixels image [cf. Fig. 1(b)]. We recall that the polar image is used to estimate the RMM and to extract the corresponding features. For the ease of visualization, the polar image is transformed to cartesian coordinates, and its pixels intensities are rescaled, thus, producing the common IVUS image. These data are exclusively used to represent the image and not for feature extraction.

B. Classification Framework

As stated previously, the weights and parameters of the mixture distribution, whose estimation was early described, are used as features to describe different types of plaque. In order to evaluate the correct modeling, we adopt a multiclass classification framework that has been successfully used in plaque characterization [12]. The role of the classification scheme is twofold: 1) it allows to evaluate the discriminative power of RMM features; and 2) it is used to support a cross-validation process, adopted to tune the L parameter (number of mixture components) in RMM model and the kernel size (image window size, where the RMM is estimated).

The classification framework is based on [12] for discriminating among fibrotic, lipidic, and calcified plaques. The multiclass problem is tackled by combining binary classifiers in the *error-correcting output codes* (ECOCs) framework [19]. In fact, ECOC is a technique to decompose a multiclass problem into several binary problems. Each binary problem is solved here by using the *adaptive boosting* (AdaBoost) classifier [20], where the weak classifiers are *decision stumps* [21].
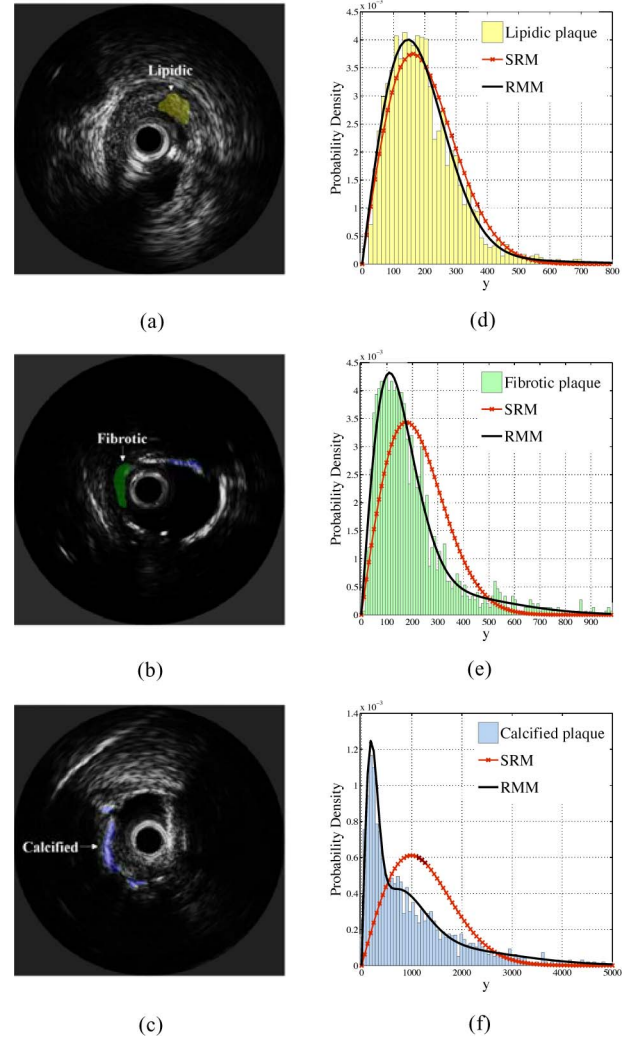

Fig. 5. (a)–(c) RMM modeling of three tissue types. (d)–(f) three-component mixture PDFs estimated for each tissue type, overlapped with single Rayleigh PDFs.

The classifier performance is evaluated by means of the *leave-one-patient-out* (LOPO) [17] cross-validation technique, where the training set is built by taking at each validation fold, all patients' data except one, used for testing. Note that each patient data may consist of different number of images (hence, different number of plaques).

Performance results are given in terms of sensitivity: $S = TP/(TP + FN)$; specificity: $K = TN/(TN + FP)$; precision: $P = TP/(TP + FP)$; and global accuracy: $A = (TP + TN)/(TP + TN + FP + FN)$, where TP = true positive, TN = true negative, FP = false positive, and FN = false negative.

C. Plaque Monolithic Description With RMM

The first experiment consists of considering a set of fibrotic, lipidic, and calcified plaques from the entire data set, according to histological analysis. Fig. 5(a)–(c) shows three examples of IVUS images containing one (or more) distinct tissue types.

TABLE I
ACCURACY VALUES FOR TUNING THE NUMBER OF MIXTURE
COMPONENTS IN RMM

LOPO	No. mixture components			
(%)	1	2	3	4
A	44.16 (36.28)	68.52 (33.29)	**85.56 (18.85)**	69.82 (31.00)

TABLE II
PERFORMANCE OF RMM, SINGLE RAYLEIGH MODEL (SRM), AND MEDIAN
FEATURES FOR MONOLITHIC CLASSIFICATION

LOPO (%)	S_{fib}	S_{cal}	S_{lip}	A
median	65.00 (39.09)	81.53 (20.34)	44.00 (37.82)	66.30 (15.92)
SRM	41.67 (46.85)	0.00 (0.00)	90.42 (15.84)	44.16 (36.28)
RMM	**91.67 (13.94)**	**93.75 (15.30)**	**82.00 (24.90)**	**85.56 (18.85)**

TABLE III
KULLBACK–LEIBLER DIVERGENCE TESTS USING RMM AND SRM:
GEOMETRIC MEAN COMPUTED OVER 67 PLAQUES

KL	Calcified	Fibrotic	Lipidic
RMM	**1.77E-4**	**7.68E-4**	**2.20E-3**
SRM	1.62E-3	4.93E-3	6.54E-3

TABLE IV
MEAN VALUES OF RAYLEIGH PARAMETERS AND MIXTURE COEFFICIENTS
ESTIMATED WITH RMM APPLIED FOR THE DATA SET OF 67 PLAQUES

RMM	Components	lipidic	fibrotic	calcified
	1	188	140	318
Rayleigh parameters	2	410	275	1171
	3	-	555	3390
	1	0.82	0.51	0.33
Mixture coefficients	2	0.18	0.39	0.46
	3	-	0.10	0.21

The purpose of the current study is to verify the ability of the RMM to describe and distinguish among the three different tissue types. In this particular experiment, the RMM algorithm is applied to the entire set of pixels enclosed in each plaque. Given this, the monolithic plaque area can be characterized by a unique set of RMM features that define a unique plaque type. Note that this situation differs from the one described in Section II-B, where the mixture model is estimated on a sliding window. This approach is used for local characterization and is further presented in the next section.

The classification framework is used to tune the parameters of the RMM method. The most critical parameter to be defined is the number of components to use in the mixture model. In order to determine the optimal L value, we use the LOPO cross-validation method, where the classification accuracy is considered as the parameter to maximize.

For each plaque, we apply the RMM algorithm, varying the number of mixture components from $L = 1$ to $L = 10$. This process results in a set of features having different lengths. For instance, for $L = 3$, we get a 7-length feature vector whereas for $L = 4$, we get a feature vector with 9 elements for each plaque. The training sets composed of RMM features created with $L = (1, \ldots, 10)$ are used in the cross-validation process. Results, reported in Table I, show that the best accuracy is achieved when three Rayleigh PDFs (components) are used in the mixture model. Hence, we can affirm that, for the specific plaque modeling application, the most suitable number of mixture components for modeling tissue echomorphology is 3. For the sake of simplicity, since classification performance decreases substantially for $L > 4$, we only show the obtained results with L varying from 1 to 4.

In order to demonstrate the effectiveness of RMM when compared to the single distribution, here termed as single Rayleigh model (SRM), or the median gray intensity, we show in Table II a comparison of these three types of features for classifying monolithic plaques. The single-parameter estimation of the SRM, obtained with the ML criterion [16], is given by $\hat{\sigma}_{\mathrm{ML}} = \sqrt{(1/2N) \sum_{i=1}^{N} y_i^2}$, where y_i is the intensity of the ith pixel within the plaque. It is clear that the application of RMM outperforms the classification results obtained with the other tested features (note that the SRM completely fails in identifying calcified plaques).

Fig. 5(d)–(f) shows normalized data histograms of lipidic, fibrotic, and calcified tissues, together with the estimated mixture (RMM) and single (SRM) distributions, respectively. Visually, the mixture model composed of three components (early determined to be the best value) describes significantly better the data when compared to the single distribution. Interestingly, as we move from lipidic to fibrotic and calcified tissue, the difference between the mixture distribution and the single distribution increases. At this point, we quantify the adequacy of the mixture model for describing each type of tissue. For this purpose, the mixture and single distributions were estimated for each plaque, and the *Kullback–Leibler* (KL) divergence [22] of such distributions with respect to the data was computed. Hence, the smaller the KL divergence is between a given distribution and the data, the more similar they are. We summarize the results by computing the geometric mean of the KL divergence for RMM and ML distributions for each plaque (see Table III).

Observations made in Fig. 5 and supported by the results presented in Table III reinforce the idea that a single distribution is not sufficient to describe the data, suggesting that different plaques types can be correctly described with different mixture distribution (and thus different RMM parameters): this fact justifies the usefulness of RMM in a tissue modeling problem.

The RMM estimation algorithm is applied to the entire data set, where for each plaque, the RMM takes into account all the pixels enclosed in it. The obtained RMM features are presented in Table IV. Particularly, it is observed that lipidic plaques are well described by two mixture components, while calcified and fibrotic plaques are modeled by three components, where the main difference lies in the range of estimated Rayleigh parameters (see Table IV). It is worth noting that in fibrotic tissue estimation, the "peakedness" of the single Rayleigh distribution is lower than the observed histogram. There is, indeed, a considerable amount of pixels with high intensity, which means that the ML parameter of the Rayleigh distribution (computed as in Section III-C) has a higher value than the expected. As a consequence, the shape of the single Rayleigh distribution will move slightly toward the right direction, as observed in Fig. 5(e). This fact enforces the need for a mixture model to correctly model tissues.

The main conclusions that can be obtained from these results are as follows.

1) Lipidic tissues are predominantly modeled by a single Rayleigh distribution (Table III: KL divergence of the same order for SRM and RMM; and Table IV: one prominent mixture component).

2) Fibrotic tissues are approximately described by a mixture model of two components.

3) Calcified tissues are better described by three Rayleigh distributions.

4) There is no significant overlapping between the range of Rayleigh parameters obtained for the lipidic and fibrotic tissues when compared to calcified tissues.

D. Plaque Local Characterization

We have established the usefulness of using a mixture of distributions to model the plaque content in a monolithic experiment. It is worth to note that, in practice, plaques are not individually segmented; thus, the RMM estimation considering all the pixels enclosed in the plaques is not generally a feasible method for plaque characterization. Nevertheless, a region of interest, which includes the plaque(s), can be at least pointed out by the physician without compromising the time of a diagnostic exam. Thus, a localwise characterization, made pixel by pixel, becomes a natural and more appropriate strategy. This strategy consists in estimating the RMM over successive processing blocks within the plaque region and assigning the RMM features to each center pixel. Subsequently, each pixel is classified into a specific tissue type (lipidic, fibrotic, or calcified) and then confronted with the ground truth.

As previously mentioned in Section II-B, in order to apply the RMM algorithm to a local analysis, we first need to define the dimension of the kernel to be used. The computational cost associated with the localwise estimation of RMM features using a processing block (kernel) of size k_s is $\mathcal{O}(2k_s)$. The tuning of this critical parameter is performed again by means of the cross-validation process. For this purpose, the RMM-based features are computed inside a kernel of size $k_s = \{2, 4, 8, 16, 24, 32\}$. Hence, six different data sets have been obtained, and for each one of them, the cross validation has been performed while varying the number of mixture components $L = \{2, 3, 4\}$. Results in terms of global accuracies are depicted in Fig. 6. Given the obtained results, $k_s = 16$ and $L = 3$ are adopted. Hence, the length of the RMM-based feature set extracted from each kernel is $2L + 1 = 7$.

In order to assess the true contribution of the proposed RMM algorithm, the plaque characterization problem is solved under three different conditions, where distinct features were computed from polar RF data (cf. Fig. 4). First, only the RMM features are used for tissue discrimination in the classification framework: the obtained classifier is here named $C.1$. Then, a set of 51 textural and spectral features presented in [12] is used to train a second classifier ($C.2$). Finally, RMM features are joined to the textural and spectral features, thus, creating a 59-element feature vector, used to train a third classifier ($C.3$).
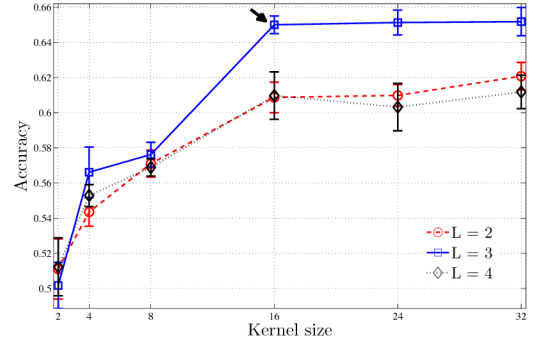

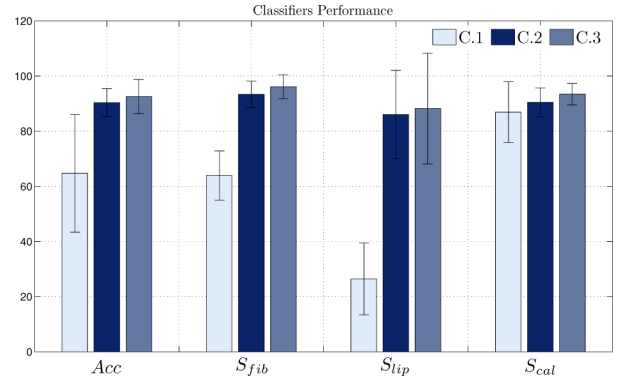Fig. 6. Classification based on RMM features according to the kernel size and number of mixture components.

Fig. 7. Bar graph comparing different classifiers ($C.1$, $C.2$, and $C.3$) according to performance measures (Acc, S_{lip}, S_{fib}, and S_{cal}).

The three classifiers are used to characterize the plaques of the database according to the LOPO technique. At each fold of both training and validation process, the data set for each kind of plaque has been randomly down sampled up to the maximum value of the less represented class over all the cases (around 2000 points per class) in order to obtain a balanced data set among classes. For each cross-validation fold, we compute the aforementioned performance criteria (cf. Section III-B); consequently, for the entire LOPO experiment (eight folds), we take the average and standard deviation of the results obtained for each fold. Classification results have been obtained by repeating 20 times the cross validation and finally by averaging the obtained performance parameters.

The comparison of $C.1$, $C.2$, and $C.3$ classifiers gives an important evidence of the effectiveness of the RMM features as well as their discriminative power. Classification results achieved with the proposed classifiers are shown in Fig. 7; a more detailed description is given in Table V.

The use of features estimated with the RMM ($C.1$) provides good results in terms of calcified and fibrotic sensitivity, and overall accuracy. A poor performance in terms of correct detection of lipidic tissue is, however, observed. Nevertheless, this is a meaningful achievement in the context of automatic plaque characterization if we consider that the dimension of the feature set is small and exclusively originated from a data source (envelope image, cf. Fig. 4). The combination of the proposed RMM features ($C.1$) with spectral and textural features [12] ($C.2$) is

TABLE V
PERFORMANCE OF PLAQUE CHARACTERIZATION: RESULTS PRESENTED AS MEAN (STD)

LOPO	$C.1$	$C.2$	$C.3$
A	64.70 (21.35)	91.37 (5.02)	**92.56 (6.18)**
S_{fib}	63.93 (8.94)	94.38 (4.79)	**96.12 (4.30)**
S_{lip}	26.41 (13.03)	87.03 (16.06)	**88.19 (20.10)**
S_{cal}	86.89 (11.02)	91.48 (5.24)	**93.42 (3.90)**
K_{fib}	74.68 (25.95)	92.49 (6.22)	**94.02 (5.32)**
K_{lip}	80.98 (14.59)	97.18 (2.85)	**97.69 (3.41)**
K_{cal}	94.27 (11.36)	95.22 (5.61)	**95.90 (6.85)**
P_{fib}	88.55 (11.28)	94.34 (6.74)	**95.69 (4.71)**
P_{lip}	86.78 (21.06)	69.26 (28.52)	**69.71 (29.94)**
P_{cal}	94.99 (8.44)	96.89 (3.59)	**96.86 (5.18)**

expected to produce improvements on the classification performance. Hence, as shown in Fig. 7 and Table V, the classifier $C.3$ yields the best classification accuracy, around 92.6%, and brings the class sensitivity up to 96.1%, 88.2%, and 93.4% for fibrotic, lipidic, and calcified plaques, respectively. This represents an improvement of more than 1% in accuracy, about 2% in fibrotic-class, more than 1% in lipidic-class and around 2% in calcified-class sensitivities, when compared to the classifier, which only considers textural and spectral features ($C.2$). These observations support the relevance of the RMM features for plaque characterization.

This result shows that features extracted from RMM are complementary to the rest of the features. Examples of plaque characterization using the $C.3$ classifier are shown in Fig. 8.

E. Statistical Analysis

In order to reinforce the usefulness of the RMM approach, we perform a test on the statistical significance of results.

To assess the statistical significance among the classifiers performance, we apply the *Friedman* and *Bonferroni–Dunn* test [23]. First of all, the ranking r_j^i for each separate classification test i and each classifier j is computed. Then, the mean ranking R_j for each one of the jth classifier is computed as $R_j = (1/\widehat{N}) \sum_{i=1}^{\widehat{N}} r_j^i$, where $\widehat{N} = M N_p$ is the total number of rounds. Obtained results are reported in Table VI; note that the best rank corresponds to the $C.3$ classifier, i.e., the classifier trained with the whole feature set.

In addition, in order to reject the *null hypothesis* that the differences on the measured classification performance are due to randomness, the *Friedman* test is performed. For this purpose, the *Friedman statistic value* is computed as follows:

$$\chi_F^2 = \frac{12\widehat{N}}{k(k+1)} \left[\sum_j R_j^2 - \frac{k(k+1)^2}{4} \right] \quad (22)$$

where $k = 3$ is the number of considered classifiers. The obtained value is $\chi_F^2 = 202.74$. As reported in [23], given the conservative property of the Friedman value, the *Iman–Davenport* correction value is preferred

$$F_F = \frac{(\widehat{N} - 1)\chi_F^2}{\widehat{N}(k-1) - \chi_F^2}. \quad (23)$$
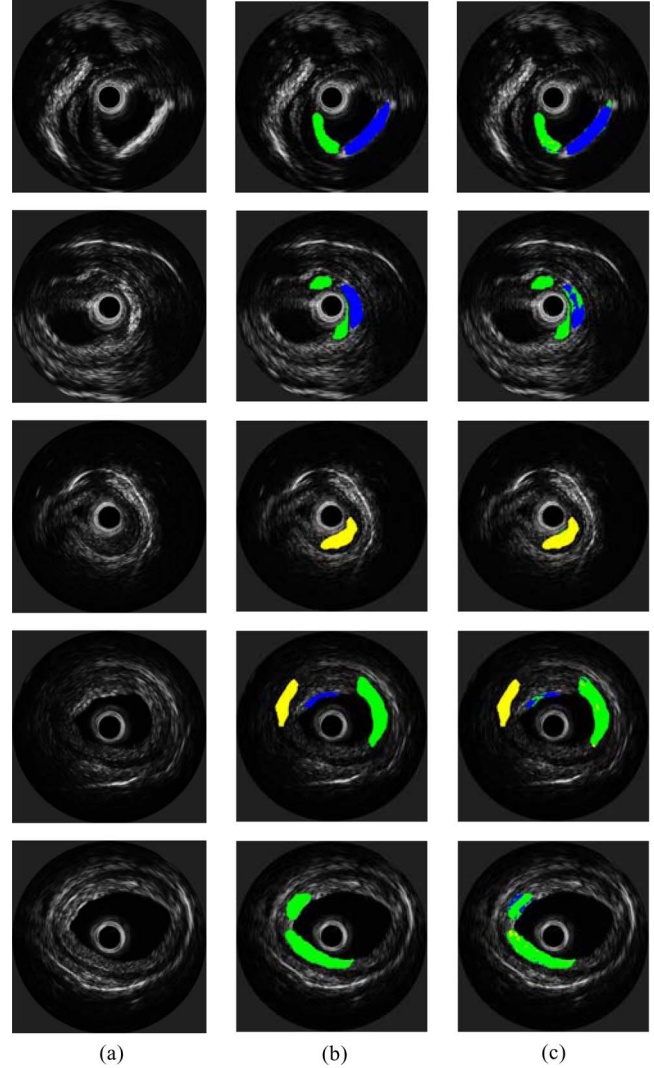

Fig. 8. Examples of plaque classification using the $C.3$ classifier. (a) IVUS images, (b) ground truth images, segmented according to the histological analysis, (c) classification. In blue (dark), green (mid gray), and yellow (light gray) are indicated calcified, fibrotic, and lipidic tissues, respectively.

TABLE VI
MEAN RANK FOR THE ACCURACY OF EACH CLASSIFIER

classifier	$C.1$	$C.2$	$C.3$
mean rank	2.8438	1.8938	**1.2625**

The value obtained in this case is $F_F = 274.9$. With three methods and a total of $\widehat{N} = 160$ experiments, F_F is distributed according to the F distribution with 2 and 318 DOF. The critical value of $F(2, \infty)$ for $\alpha = 0.05$ is 2.99. Since the obtained value for F_F is higher than the critical value, the null hypothesis is rejected, i.e., the differences in the obtained results are not due to randomness.

Once the null hypothesis has been rejected, we check if the classifier $C.3$, resulting in the best discriminative power, is significantly better than the other classifiers. For this purpose, the *Bonferroni–Dunn* test [23] is performed: the performance of two classifiers is significantly different if the corresponding average
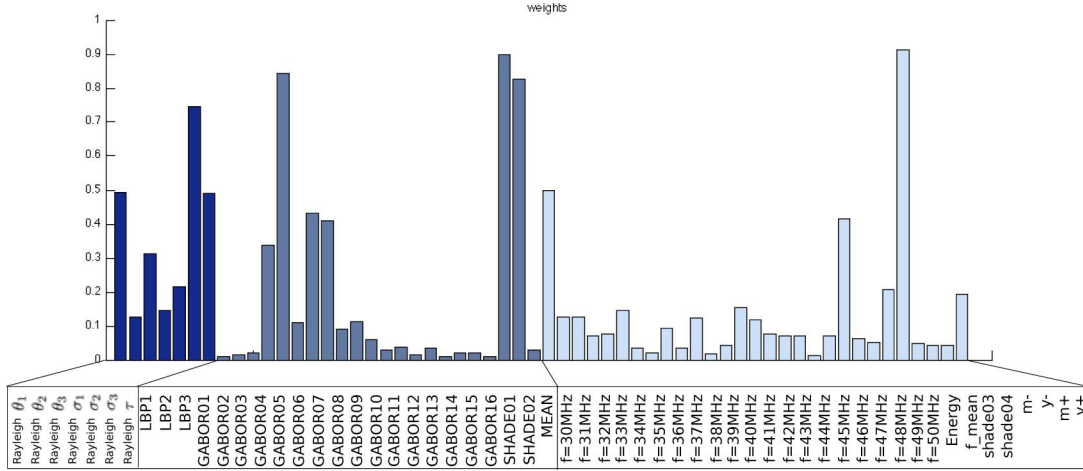
Fig. 9.   Analysis of the normalized weight for each feature of the $C.3$ classifier.

ranks differ by at least the *critical difference*

$$\mathrm{CD} = q_\alpha \sqrt{\frac{k(k+1)}{6\widehat{N}}} \qquad (24)$$

where q_α is based on the studentized range statistic divided by $\sqrt{2}$. Since our goal is the comparison of the $C.3$ classifier with respect to the others, the *Bonferroni–Dunn* test is suitable, and a correction factor must be considered in the q_α value (cf. [23] for details). In our case, we obtain CD = 0.2949, which is smaller than each difference among the mean rank of the classifier $C.3$ and the rank of each other classifier. For this reason, we can infer that the classifier is significantly better than the rest with a confidence of 95%.

F. Features Weight Analysis

Finally, we want to evaluate the importance of the included features in the quality of the classifier $C.3$. The AdaBoost algorithm assigns a certain weight to each weak classifier selected at each round during the training process [20]. Since the decision stump weak classifier is only related to a single feature [21], we can use the weight assigned by AdaBoost to evaluate the importance of each feature during the training process. Note that each feature can be selected more than one time: in that case, the sum of each weight for a specific feature is considered. Let us define N_P the number of *in vitro* cases, N_F the number of features, K the number of binary problems, $f = 1, \dots, N_F$ the index of each feature, $k = 1, \dots, K$ the index of each binary problem, N_R the number of rounds by whose the computation has been repeated, and $\alpha_{k,p,r}^f$ the weight assigned to the fth feature. The normalized weight assigned by AdaBoost to each feature can be computed as $W_f = \max\{w_f^1, \dots, w_f^1\}$, where

$$w_f^k = \frac{1}{N_P N_R} \sum_{p=1}^{N_P} \sum_{r=1}^{N_R} \frac{\alpha_{k,p,r}^f}{\max\{\alpha_{k,p,r}^1, \dots, \alpha_{k,p,r}^{N_F}\}}. \qquad (25)$$

Fig. 9 represents the normalized weights of each feature. It is worth to note the importance given by the classifier to the RMM features, particularly to feature 1 first Rayleigh parame-

ter), feature 6 (third mixture coefficient), and feature 7 (number of effective mixture components). Given the high discriminative power of the $C.3$ classifier, the expressive weights assigned to the RMM-based features corroborate the importance of the RMM model as well as its capability for discriminating different tissues. The information provided about the most discriminant features may be used on a feature-selection procedure in future work related to tissue characterization.

IV. CONCLUSION

This paper proposes a method for plaque characterization in IVUS data based on a mixture of Rayleigh distributions. The coefficients and parameters of the mixture model are used as features for describing fibrotic, lipidic, and calcified plaques.

The RMM algorithm was evaluated and tuned using a classification framework based on a multiclass problem applied to a validated IVUS data set and following a cross-validation strategy. Results suggest that the optimal RMM method for plaque characterization consists of $L = 3$ mixture components and should be computed on a kernel of size $k_s = 16$.

First, the true value of RMM features for tissue characterization was evaluated through a plaque monolithic problem using a cross-validation strategy, providing a global accuracy of 86%. This result highlights the relevance of RMM features for discriminating among the three different types of tissue.

Furthermore, the method was evaluated on a localwise classification problem when using only the RMM tuned features and when combining them with textural and spectral features used in an authors' previous study. The inclusion of RMM features demonstrates to generally improve the classification performance up to a global accuracy of 92.6%. According to the most significant performance parameters, such as accuracy and class sensitivity, fusing RMM features with textural and spectral features represents a general improvement of more than 1%, and in some cases about 2%.

Finally, statistical analysis using the *Friedman and Bonferroni–Dunn* shows that the classifier, which includes

RMM, and textural and spectral features, is significantly better than the other studied ones, thus, reinforcing the significance of the obtained improvement when using RMM features.

The method is intended to characterize tissues enclosed in a previously segmented plaque. Moreover, automatic segmentation capabilities can be potentially achieved by classifying the whole image and then by postprocessing the labeled regions. Without a deep analysis on features similarities between different vessel areas, the classification result on regions different from plaques cannot be stated. Indeed, it can be guessed that, at least for what concerns the textural features, regions enclosing struts (in presence of stent) can be classified as calcified plaque, and the whole adventitia layer as fibrotic plaque. No guessing can be done for the blood region.

Hence, we have shown that the RMM has a high impact on plaque characterization and could significantly contribute to a more accurate study of plaque composition, and consequently to an objective identification of vulnerable plaques.

References

[1] L. Spagnoli, A. Mauriello, and G. Sangiorgi, "Extracranial thrombotically active carotid plaque as a risk factor for ischemic stroke," *J. Amer. Med. Assoc.*, vol. 292, pp. 1845–1852, 2004.

[2] T. L. Szabo, *Diagnostic Ultrasound Imaging: Inside Out*. New York: Academic, 2004.

[3] C. Burckhardt, "Speckle in ultrasound B-mode scans," *IEEE Trans. Sonics Ultrason.*, vol. SU-25, no. 1, pp. 1–6, Jan. 1978.

[4] J. Thijssen, "Ultrasonic speckle formation, analysis and processing applied to tissue characterization," *Pattern Recognit. Lett.*, vol. 24, no. 4/5, pp. 659–675, 2003.

[5] T. Eltoft, "Modeling the amplitude statistics of ultrasonic images," *IEEE Trans. Med. Imag.*, vol. 25, no. 2, pp. 229–240, Feb. 2006.

[6] E. Brusseau, C. de Korte, F. Mastik, J. Schaar, and A. van der Steen, "Fully automatic luminal contour segmentation in intracoronary ultrasound imaging—A statistical approach," *IEEE Trans. Med. Imag.*, vol. 23, no. 5, pp. 554–566, May 2004.

[7] R. W. Prager, A. H. Gee, G. M. Treece, and L. Berman, "Decompression and speckle detection for ultrasound images using a homodyned K distribution," *Pattern Recognit. Lett.*, vol. 24, no. 4/5, pp. 705–713, Feb. 2003.

[8] E. Jakeman, "Speckle statistics with a small number of scatterers," *Opt. Eng.*, vol. 23, no. 4, pp. 453–461, 1984.

[9] V. Dutt and J. F. Greenleaf, "Ultrasound echo envelope analysis using a homodyned K distribution signal model," *Ultrason. Imag.*, vol. 16, no. 4, pp. 265–287, 1994.

[10] P. Shankar, "Ultrasonic tissue characterization using a generalized Nakagami model," *IEEE Trans. Ultrason., Ferroelectr. Freq. Control*, vol. 48, no. 6, pp. 1716–1720, Nov. 2001.

[11] K. Sorensen and S. Andersen, "Rayleigh mixture model-based hidden Markov modeling and estimation of noise in noisy speech signals," *IEEE Trans. Audio, Speech, Lang. Process.*, vol. 15, no. 3, pp. 901–917, Mar. 2007.

[12] F. Ciompi, O. Pujol, C. Gatta, O. Rodriguez, F. Mauri, and P. Radeva, "Fusing in-vitro and in-vivo intravascular ultrasound data for plaque characterization," *Int. J. Cardiovasc. Imag.*, vol. 26, no. 7, pp. 763–779, 2010.

[13] C. Sehgal, "Quantitative relationship between tissue composition and scattering of ultrasound," *Acoust. Soc. Amer. J.*, vol. 94, pp. 1944–1952, Oct. 1993.

[14] A. P. Dempster, N. M. Laird, and D. B. Rdin, "Maximum likelihood from incomplete data via the EM algorithm," *J. Roy. Statist. Soc., Ser. B*, vol. 39, pp. 1–38, 1977.

[15] G. Hadley, *Nonlinear and Dynamic Programming*. Reading, MA: Addison-Wesley, 1964.

[16] J. Harris and H. Stocker, "Maximum likelihood method," in *Handbook of Mathematics and Computational Science*. New York: Springer-Verlag, 1998, p. 824.

[17] K. L. Caballero, J. Barajas, O. Pujol, O. Rodriguez, and P. Radeva, "Using reconstructed IVUS images for coronary plaque classification," in *Proc. IEEE Eng. Med. Biol. Conf.*, Lyon, France, pp. 2167–2170.

[18] M. Rosales and P. Radeva, "A basic model for IVUS image simulation," in *Handbook of Biomedical Image Analysis* (Topics in Biomedical Engineering International Book Series). New York: Springer-Verlag, 2005, pp. 1–55..

[19] T. G. Dietterich and G. Bakiri, "Solving multiclass learning problems via error-correcting output codes," *J. Artif. Intell. Res.*, vol. 2, pp. 263–286, 1995.

[20] R. E. Schapire, "Using output codes to boost multiclass learning problems," in *Proc. 14th Int. Conf. Mach. Learning*. Nashville, TN: Morgan Kaufmann, 1997, pp. 313–321.

[21] J. Rennie, "Boosting with decision stumps and binary features," Massachusetts Inst. Technol., Cambridge, MA, Tech. Rep., 2003.

[22] T. Cover and J.A Thomas, *Elements of Information Theory*. New York: Wiley-Interscience, 1991.

[23] J. Demšar, "Statistical comparisons of classifiers over multiple data sets," *J. Mach. Learning Res.*, vol. 7, pp. 1–30, 2006.

José C. Seabra (M'09) received the M.Sc. degree from the Universidade Técnica de Lisboa, Lisbon, Portugal, in 2007. He is currently working toward the Ph.D. degree in biomedical engineering at the Institute for Systems and Robotics in collaboration with the University of Lisbon Medical School and Computer Vision Center, Barcelona, Catalonia, Spain.

He is engaged in research on medical image processing, particularly in computer-aided diagnosis of carotid atherosclerosis using ultrasound. His research interests include medical imaging, 3-D ultrasound, denoising, and texture analysis.

Francesco Ciompi received the M.S. degree in electronic engineering from the Università di Pisa, Pisa, Italy, in 2006, and the M.S. degree in computer vision and artificial intelligence from the Universitat Autónoma de Barcelona, Catalonia, Spain, in 2008. He is currently working toward the Ph.D. degree in the Department of Applied Mathematics and Analysis, Universitat de Barcelona, Catalonia.

His research interests include the use of machine learning techniques for the classification and segmentation of intravascular ultrasound data.

Oriol Pujol has been an Associate Professor at the Department of Applied Mathematics and Analysis, University of Barcelona, Catalonia, Spain, and a Senior Researcher at the Computer Vision Center, Universitat Autónoma de Barcelona, Catalonia since 2008. Since 2004, he has been an active member in the organization of several activities related to image analysis, computer vision, machine learning, and artificial intelligence. In applied research, he has been engaged in medical image analysis, object recognition, wearable computing, and augmented reality.

Josepa Mauri received the M.D. degree from the Universitat Autònoma de Barcelona, Catalonia, Spain, in 1982, and the Laurea summa Cum Laude in medicine from the Universitat de Barcelona, Catalonia, in 1992.

Since 2000, she has been the Director of the Cardiac Catherization Laboratory, Hospital Universitari "Germans Trias I Pujol de Badalona," Catalonia. Her clinical research interests include coronary angioplasty and dilated cardiomyopathy, dilated cardiomiopathy, coronary angioplasty, stents, endothelial disfunction, and intravascular ultrasound studies. She is currently involved in international educational projects in interventional cardiology.

Dr. Mauri was the President of the Diagnostic Intracoronary Technics/IVUS Working Group of the Spanish Society of Cardiology from 2002 to 2005, and of the Spanish Working Group in Cardiac Interventions of the Spanish Society of Cardiology from 2006 to 2009.

João Sanches (M'06) received the E.E., M.Sc., and Ph.D. degrees from the Technical University of Lisbon, Lisbon, Portugal, in 1991, 1996, and 2003, respectively.

He is currently an Assistant Professor in the Electrical and Computer Engineering Department, Instituto Superior Técnico, Universidade Técnica de Lisboa,Lisbon, where he is also a Researcher at the Institute for Systems and Robotics. His main research interests include biomedical engineering. Ultrasound, fMRI, and fluorescence confocal microscopy imaging are some of the biological and medical image modalities, where he works in collaboration with the Medical School, Hospital de Santa Maria, Lisbon.

Dr. Sanches is a member of the IEEE Engineering in Medicine and Biology Society and of the Bio Imaging and Signal Processing Technical Committee of the IEEE Signal Processing Society.

Petia Radeva (M'01) received the Ph.D. degree from the Universitat Autònoma de Barcelona, Catalonia, Spain, in 1998.

She is currently a Senior Researcher at the Universitat de Barcelona, Catalonia. She is the author or coauthor of more than 150 publications in international journals and proceedings, and has 12 patents in the field of medical imaging. Her current research interests include the development of learning-based approaches (in particular statistical methods) for computer vision and medical imaging. She has led one EU project and several Spanish projects. She is the Head of the projects in cardiac imaging and wireless endoscopy in collaboration with Spanish hospitals and international medical imaging companies.